Supplementary Information for:
Ultrafast metal-to-ligand charge transfer driven by bond shortening revealed with dual-edge computational X-ray spectroscopy

Sheng-Yu Wang,[1,2] Jun-Rong Zhang,[2] Guoyan Ge,[2] and Weijie Hua[2]
[1]*School of Physics and Electronic Engineering,*
Research Institute of Optoelectronic Functional Materials,
Jining University, Qufu, Shandong 273155, China
[2]*MIIT Key Laboratory of Semiconductor Microstructure and Quantum Sensing,*
Department of Applied Physics, School of Physics,
Nanjing University of Science and Technology, 210094 Nanjing, China

(Dated: October 15, 2025)

Contents

Supplementary Notes

Note 1. Triplet Ground State Validation

The ground-state spin multiplicity of CuO_2^+ was determined by comparing the energies of the singlet, triplet, and quintet states. As summarized in Table S1, B3LYP calculations at the respective optimized geometries show that the triplet state is the most stable, with energies 0.44 eV lower than the singlet and 3.71 eV lower than the quintet.

To further validate this assignment, single-point energy calculations were performed using both B3LYP and RASPT2 methods at two key geometries: the triplet-optimized structure (**2b**) and the experimental structure (**2a**). The results, presented in Table S2, show consistent energy ordering across both methods. In all cases, the triplet state is energetically favored over the singlet, providing robust confirmation of the triplet ground state assignment.

Note 2. Supplementary Analyses

A. Impact of Core Holes on DFT Energy Levels

To elucidate the electronic structure of CuO_2^+ and investigate core-hole effects, we computed energy level diagrams for three distinct states at structure **2a**: the ground electronic state, a full core-hole (FCH) state with an O 1s hole localized on O2 (see Fig. 1a), and an FCH state with a Cu $2p_y$ core hole. These calculations were performed using the Q-Chem[1] package with unrestricted DFT and the ωB97M-V functional[2]. A mixed basis set was employed, utilizing def2-QZVP[3] for O2 and def2-TZVP[4] for O1 and Cu to enhance the localization of degenerate O 1s orbitals. In all core-hole calculations, the hole was assigned to the β spin.

Figure S1 presents the ground-state energy level alongside MOs. The substantial HOMO–LUMO gaps (10.8 eV for α-spin, 10.5 eV for β-spin) signify a highly stable electronic configuration. The minimal spin polarization (0.3 eV difference between spin channels) indicates nearly degenerate orbital energy landscapes. This electronic structure is characteristic of a strongly bonded triplet ground state, wherein the two unpaired electrons occupy near-degenerate singly occupied molecular orbitals (SOMOs) 22α and 23α.

This description is consistent with multiconfiguration calculations (Section Note 2 B, Table S3), which show that both orbitals have occupations near unity. Furthermore, the three key frontier MOs–the Cu $3d_{xz}$–O2 π^*_{ip} bond (23α, 22β), the O2 π^*_{oop} orbital (22α, 23β), and the Cu $3d_{xz}$+O2 π^*_{ip} antibond (17α, 19β)–are located near the frontier in each spin channel and align with the active orbitals identified in the multiconfigurational analysis.

Figure S2 compares the ground-state energy levels with those of the O 1s and Cu $2p_y$ FCH states, revealing significant core-hole effects. The difference between the α and β HOMO-LUMO gaps differs by 0.3 eV in the ground state but increases to 3.0 eV for the O 1s core hole and 0.6 eV for the Cu $2p_y$ core hole. The more substantial effect of the O 1s core hole is attributed to symmetry lowering from C_{2v} to C_s, while the symmetry of the Cu $2p_y$ state remains unchanged. This element-specific core-hole effect is further evidenced by irregularities in MO shapes (Fig. S2b), indicating a significant deviation in valence electron distribution symmetry due to the absence of a core electron.

In addition to affecting the HOMO-LUMO gap and MO symmetry, core holes can alter the order of MOs. For the β spin orbitals d_{xz}-π^*_{ip} and π^*_{oop}, the O 1s core hole causes an inversion in their energy levels, while the Cu $2p_y$ core hole preserves the ground-state order.

This behavior may also be linked to the symmetry change. In both FCH states, the order of these orbitals aligns with trends observed in the XAS spectra at the O K-edge (Fig. 3) and Cu $L_{2,3}$-edge (Fig. 4).

B. Active Orbitals and Their Occupation Number Changes

This section examines the changes in occupation numbers of active orbitals critical for understanding the electronic structure of CuO_2^+. The selection of active orbitals is guided by including Cu 3d and O_2 $2p$ orbitals, which accurately capture key interactions. For structure **2a**, we visualize eight active RAS2 orbitals at the converged state-averaged RASSCF wavefunction, as shown in Fig. S3a. These orbitals serve as the initial guess for subsequent calculations, including those for Cu $2p$ core-excited states (Fig. S3b). While most active orbitals effectively represent the valence state, noticeable changes in their occupation numbers are observed.

The RASSCF occupation numbers for the eight RAS2 orbitals (MOs 18-25) of $CuO2^+$ in its triplet ground state, evaluated at varying Cu-O distances, are detailed in Table S3. Among these, three critical orbitals are identified: MO 20 ($d_{xz}+\pi^*_{\mathrm{ip}}$), MO 22 ($\pi^*_{\mathrm{oop}}$), and MO 23 ($d_{xz}-\pi^*_{\mathrm{ip}}$). The partial occupation of approximately 1 for the antibonding orbitals (MOs 22 and 23) indicates significant static correlation. The persistent occupation of around 2.0 for the bonding orbital (MO 20) and approximately 1.0 for the antibonding orbital (MO 23) highlights a strongly correlated electron pair. This correlated pair is essential for the multi-configurational description of the Cu-O bond, thereby justifying the inclusion of both orbitals in the active space despite the integer occupation of MO 20.

C. Metal-to-Ligand Charge Transfer Analysis

Figure S4 presents the natural population analysis (NPA) charges for the Cu and O2 units of CuO_2^+ computed at the RASPT2 level across a range of Cu–O bond lengths. The systematic evolution of these charges along the binding coordinate demonstrates a gradual MLCT as the bond shortens. Quantitatively, the analysis indicates a net electron transfer of approximately $0.2e$ from structure **2b** ($q_{\mathrm{Cu}} = 1.0\ e$, $q_{\mathrm{O}_2} = -0.2\ e$) to **2a** ($q_{\mathrm{Cu}} = 1.2\ e$, $q_{\mathrm{O}_2} = -0.4\ e$).

D. Composition Analysis of Natural Transition Orbitals

Table S4 presents the composition analysis for particle SO-NTOs in the Cu $L_{2,3}$-edge XAS spectrum at **2a**. The C-squared population analysis (SCPA) method, also known as the Ros-Schuit method[5], was employed with a threshold for the MO coefficient of $|C_i| > 0.5\%$. The main peaks at 931.8 eV (state 21) and 951.1 eV (state 146) arise from Cu $2p \rightarrow 3d$ transitions, exhibiting 21% Cu $3d$ character and 77% O $2p$ contributions. The weaker features at 933.6 eV (state 43), 936.6 eV (state 72), and 943.1 eV (state 114) are attributed to Cu $2p \rightarrow 4s$ transitions, which display dominant Cu $4s$ character (83.8–85.1%) and minimal O $2p$ contributions (4.8–6.1%).

The composition analysis was extended to include multiple structures between **2a** and **2b**. Table S5 illustrates the evolution of orbital contributions as Cu–O bond lengths increase. The Cu $3d$ character in the major transitions (peaks i and n) decreases monotonically from 21% to complete disappearance, while the O $2p$ contributions rise from 77% to 94%. In the satellite features (peaks k, l, m, and p), the Cu 4s character systematically increases from 84–85% to 88–92% with bond elongation. This progressive shift in orbital composition indicates a weakening of the metal-ligand interaction at longer bond distances, where the Cu 3d–O 2p hybridization diminishes, allowing the more diffuse Cu 4s orbitals to play a relatively larger role in the excited states.

Note 3. Supplementary Validations

A. Structural Input Dependence

Two experimental $LCuO_2$ structures with similar CuO_2 core geometries were reported: Reynolds *et al.*'s anilido-imine complex (1.82/1.83 Å Cu-O, 1.83/1.86 Å Cu-N) [6] and Aboelella *et al.*'s methyldiiminato analogue (uniform 1.82 Å Cu-O, 1.86 Å Cu-N) [7], both showing 1.39 Å O-O distances (Fig. S5). Notably, a subsequent XAS study by Sangari et al.[8] indexed both structures under the same compound designation.

While our prior study [9] used Reynolds' structure, we now employ Aboelella's symmetric variant to simplify the dependence on one varying structure parameter $r_{\text{Cu-O}}$. To validate, RASPT2 simulations of Cu $L_{2,3}$-edge XAS for both structures were performed, yielding largely similar spectra (Fig. S5). Minor intensity differences at 938 and 957 eV reveal spectral sensitivity to structural variations, while both simulated spectra reproduce the experimental data [8]. We therefore adopt Aboelella's $LCuO_2$ structure [7] (denoted **1**) as the starting geometry for CuO_2^+ (**2a**, with ligand L^- removed), as this choice does not affect our conclusions.

B. Assessment of Multiconfigurational Parameters

To optimize our multiconfigurational approach for Cu $L_{2,3}$-edge spectra, we systematically evaluated: (1) dynamic correlation (RASPT2 vs. RASSCF), (2) basis sets, (3) state averaging (n_v=5–100, n_c=0–100), and (4) RAS2 active space size (n_A=2–8). Each test was conducted while keeping other parameters constant. Figures S6–S10 illustrate the following findings:

Minimal Sensitivity to Dynamic Correlation. RASPT2 and RASSCF yield nearly identical spectra (Fig. S6), differing only slightly in spectral profiles while maintaining nearly equal energy positions.

Basis Set Dependence. Although VDZP was ultimately selected, larger basis sets enhance absolute energy precision without significantly altering spectral shapes (Fig. S7).

Robustness to State Averaging. Spectra show negligible variation across the tested ranges of n_v (5–100, Fig. S8) and n_c (0–100, Fig. S9). Optimal values (n_v=5, n_c=40) ensure convergence.

Active Space Sensitivity. While n_A=6 and 8 produce qualitatively similar spectra (Fig. S10), the larger active space better resolves minor peaks. We have adopted n_A=6 for a balance of accuracy and cost.

These systematic validations confirm the excellent method robustness for simulating Cu L-edge spectra of CuO_2^+, despite the absence of experimental results thus far.

Supplementary Tables

TABLE S1: **DFT energies at optimized geometries**. Total energies (in a.u.) of CuO_2^+ at the optimized geometries for different spin states, computed using B3LYP. Relative energies (in eV, in parentheses) are given with respect to the triplet ground state (structure **2b**).

Singlet	Triplet	Quintet
-346.14637 (0.44)	-346.16264 (0.00)	-346.02638 (3.71)

TABLE S2: **Single-point energies across methods**. Total energies (in a.u.) of CuO_2^+ for the lowest singlet and triplet states at structures **2a** and **2b**, computed using RASPT2 and B3LYP. Relative energies (in eV) are shown in parentheses, referenced to the respective triplet state energy at each geometry.

CuO_2^+	Method	Singlet	Triplet
2a	RASPT2	-1803.37866 (0.66)	-1803.40307 (0.00)
	B3LYP	-346.10882 (0.44)	-346.12497 (0.00)
2b	RASPT2	-1803.39052 (0.92)	-1803.42433 (0.00)
	B3LYP	-346.10716 (1.51)	-346.16264 (0.00)

TABLE S3: **Active orbital occupations**. RASSCF occupation numbers for the eight RAS2 orbitals (MOs 18-25) of CuO_2^+ in its triplet ground state at varying Cu-O distances ($r_{\text{Cu-O}}$, Å). The RAS2 orbitals at structure **2a** ($r_{\text{Cu-O}} = 1.82$ Å) are visualized in Fig. S3(a). Critical orbitals are highlighted in bold: MOs 20 ($d_{xz} + \pi^*_{\text{ip}}$), 22 ($\pi^*_{\text{oop}}$), and 23 ($d_{xz} - \pi^*_{\text{ip}}$).

$r_{\text{Cu-O}}$	18	19	**20**	21	**22**	**23**	24	25
1.82	1.95	1.92	1.99	1.95	1.05	1.04	0.02	0.08
1.89	1.95	1.93	1.99	1.95	1.05	1.04	0.02	0.07
1.96	1.95	1.93	2.00	1.95	1.05	1.04	0.02	0.07
2.03	1.95	1.94	2.00	1.95	1.05	1.04	0.02	0.06
2.10	1.95	1.94	2.00	1.95	1.04	1.04	0.02	0.06
2.17	1.96	1.95	2.00	1.95	1.04	1.04	0.02	0.05
2.24	1.96	1.96	2.00	1.95	1.04	1.03	0.01	0.05

TABLE S4: **NTO composition at 2a**. Composition analysis of particle SO-NTOs for structure **2a**, with state indexes corresponding to labeled peaks in the Cu $L_{2,3}$-edge XAS spectra [Fig. 2(e)]. Peak energies (eV) and assignments are included.

SO-state	Energy	Composition (%)			Assignment
		Cu $3d$	Cu $4s$	O $2p$	
21	931.8	21.4	–	77.4	Cu $3d_{xz} - \pi^*_{\text{ip}}$
31	933.1	0.6	–	99.2	π^*_{oop}
43	933.6	0.6	83.8	6.1	Cu $4s$
72	936.6	–	85.1	4.8	Cu $4s$
83	937.1	5.4	7.1	83.2	Cu $3d - \pi_{\text{ip}}$
114	943.1	–	85.1	4.8	Cu $4s$
146	951.1	21.4	–	77.4	Cu $3d_{xz} - \pi^*_{\text{ip}}$
151	952.6	0.6	–	99.2	π^*_{oop}
154	952.9	0.6	83.8	6.1	Cu $4s$

TABLE S5: **NTO composition evolution**. Composition analysis (%) of particle SO-NTOs for selected CuO_2^+ structures between **2a** ($r_{\text{Cu-O}} = 1.82$ Å) and **2b** ($r_{\text{Cu-O}} = 2.24$ Å). Peaks correspond to features in Cu $L_{2,3}$-edge XAS spectra [Fig. 4(a)].

$r_{\text{Cu-O}}$	i			j			k			l		
	d	s	p	d	s	p	d	s	p	d	s	p
1.82	21$\downarrow$	–	77$\uparrow$	0.6$\downarrow$	–	99$\uparrow$	0.6$\downarrow$	84$\uparrow$	6$\downarrow$	–	85$\uparrow$	5$\downarrow$
1.96	15	–	84	–	–	100	0.5	86	6	–	88	5
2.10	5	–	93	–	–	100	–	88	6	–	90	4
2.24	–	–	95	–	–	–	–	92	4	–	92	4

$r_{\text{Cu-O}}$	m			n			o			p		
	d	s	p	d	s	p	d	s	p	d	s	p
1.82	–	85$\uparrow$	5$\downarrow$	21$\downarrow$	–	77$\uparrow$	0.6$\downarrow$	–	99$\uparrow$	0.6$\downarrow$	84$\uparrow$	6$\downarrow$
1.96	–	88	5	15	–	84	–	–	100	0.5	86	6
2.10	–	90	4	6.5	–	93	–	–	–	–	88	6
2.24	–	92	4	4.9	–	94	–	–	–	–	91	5

[a] Entries marked "–" indicate components <4.0%.

[b] Symbols ↑/↓ track component increases/decreases with Cu–O bond length.

[c] All values are percentages. d = Cu $3d$, s = Cu $4s$, p = O $2p$ orbitals.

Supplementary Figures

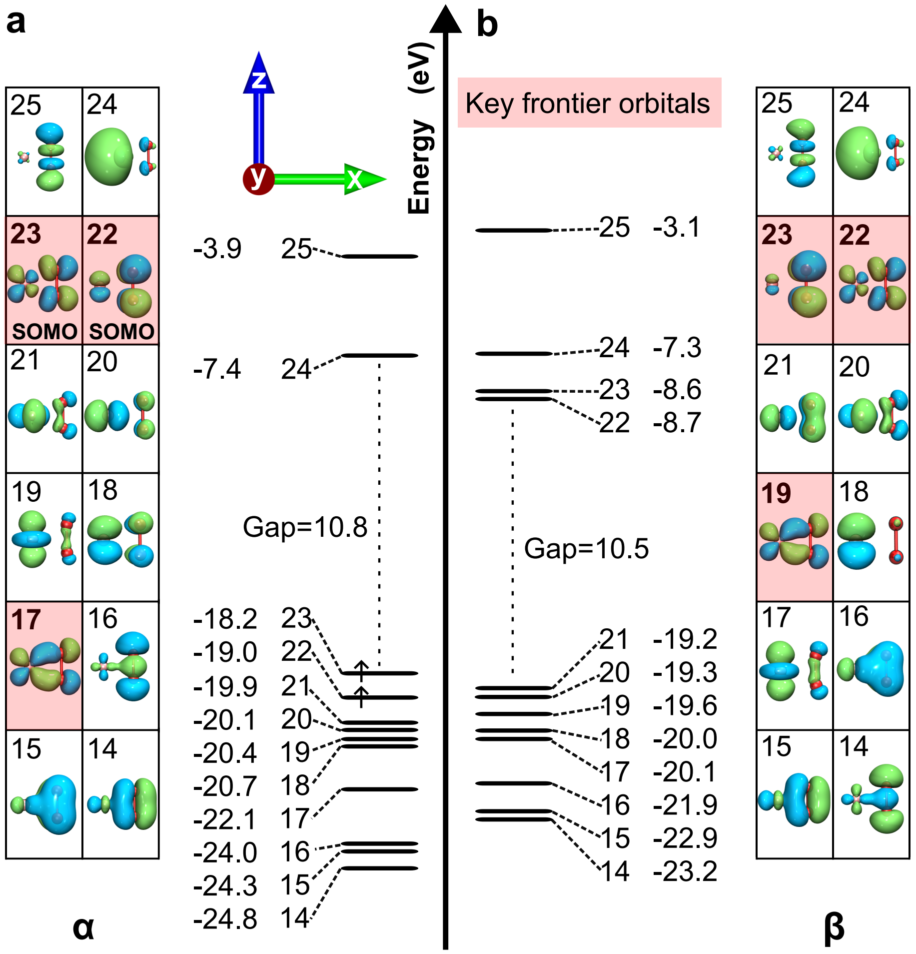

FIG. S1: **Ground state electronic structure.** Unrestricted DFT (ωB97M-V) computed molecular orbital energy level diagram for the triplet ground state of structure **2a**. Arrows indicate SOMOs. MOs are depicted adjacent to their corresponding energy levels with the three key frontier orbitals highlighted (bold, red) for each spin channel: Cu $3d_{xz}$–O_2 π^*_{ip} (23α, 22β), π^*_{oop} (22α, 23β), and Cu $3d_{xz}$+O_2 $\pi^*_{\mathrm{ip}}O_2$ (17α, 19β). The HOMO–LUMO gap for each spin is indicated (in eV).

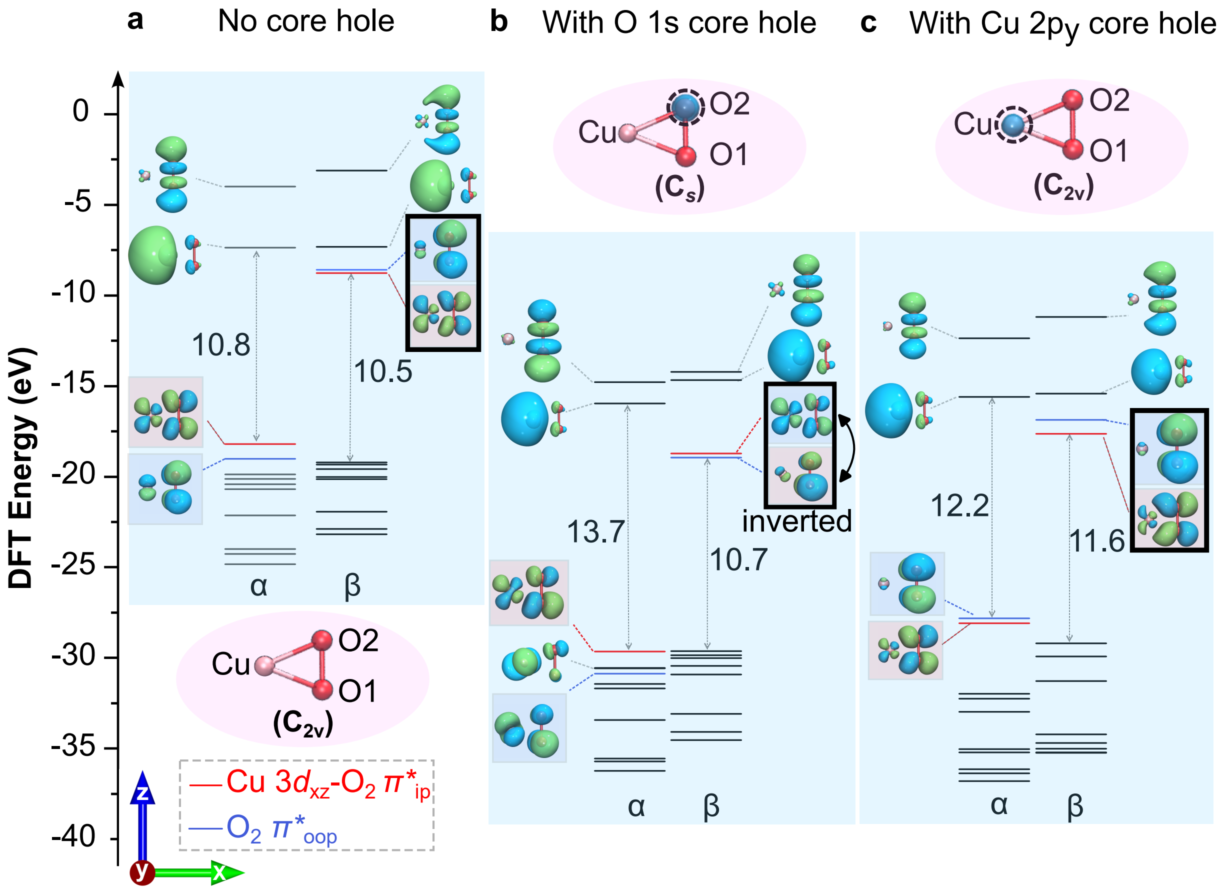

FIG. S2: **Core-hole effects on electronic structure.** Unrestricted DFT (ωB97M-V) computed molecular orbital energy level diagrams for structure **2a**: (a) ground electronic state (triplet), (b) FCH state with an O 1s core hole (quartet), and (c) FCH state with a Cu $2p_y$ core hole (quartet). Two critical orbitals are highlighted: Cu $3d_{xz}$–O_2 π^*_{ip} (red) and O_2 π^*_{oop} (blue). In each panel, molecular symmetry is labeled. An energy level inversion occurs in the β-spin channel (hosting the core hole) in (b). Several additional frontier MOs are also depicted.

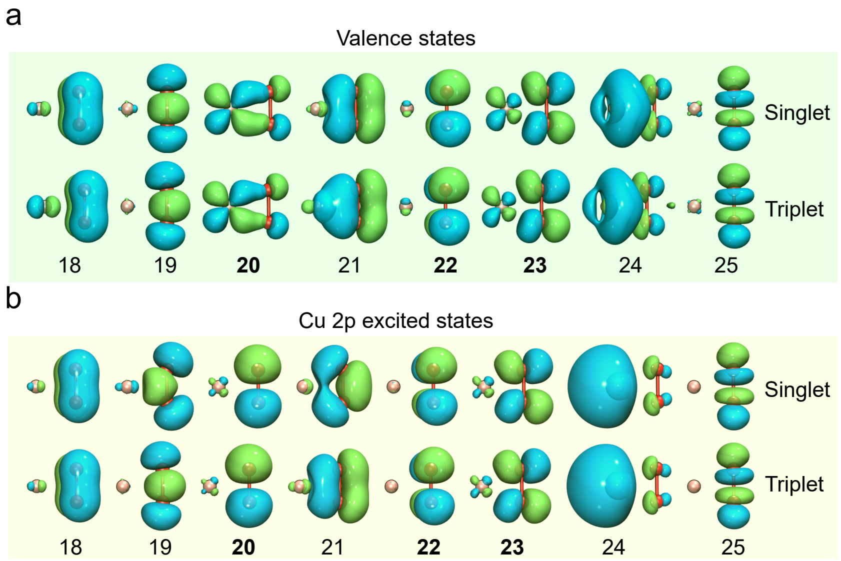

FIG. S3: **Active space orbitals.** Convergent RAS2 active orbitals of $CuO_2{}^+$ structure **2a** from state-averaged RASSCF calculations for (a) 5 valence and (b) 40 Cu $2p$ core-excited states. Critical orbitals are highlighted: MOs 20 ($d_{xz} + \pi^*_{\rm ip}$), 22 ($\pi^*_{\rm oop}$), and 23 ($d_{xz} - \pi^*_{\rm ip}$).

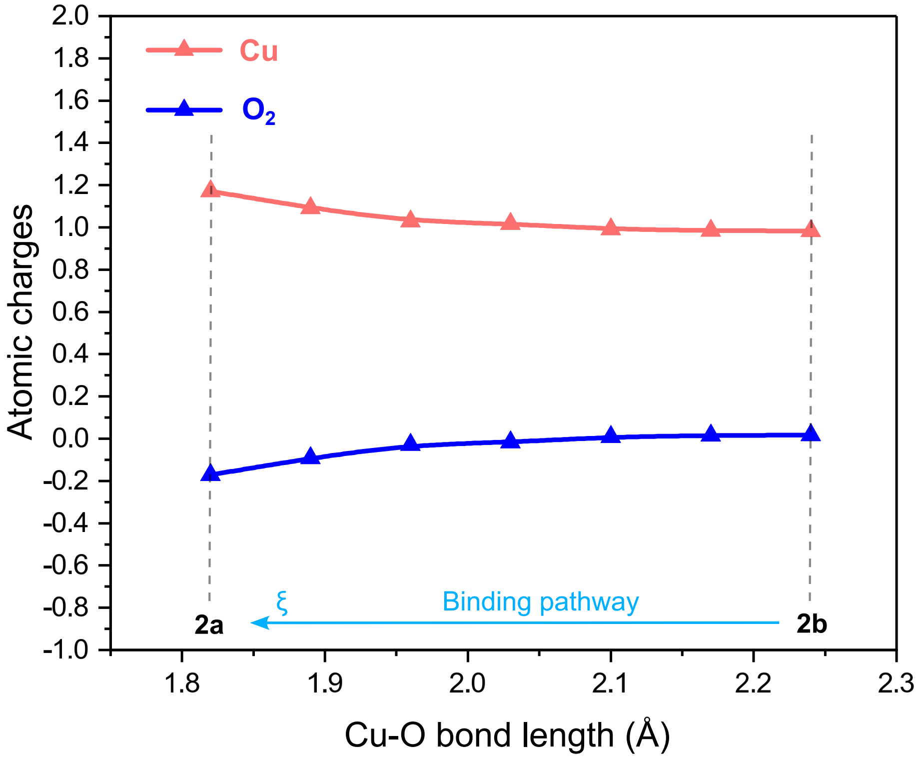

FIG. S4: **Metal-to-ligand charge transfer evolution.** Natural population analysis charges for Cu and O_2 fragments in CuO_2^+ as a function of Cu–O distance. The systematic charge evolution from structure **2b** (2.24 Å) to **2a** (1.82 Å) indicates a net metal-to-ligand charge transfer of 0.2e. Calculations performed at the RASPT2 level.

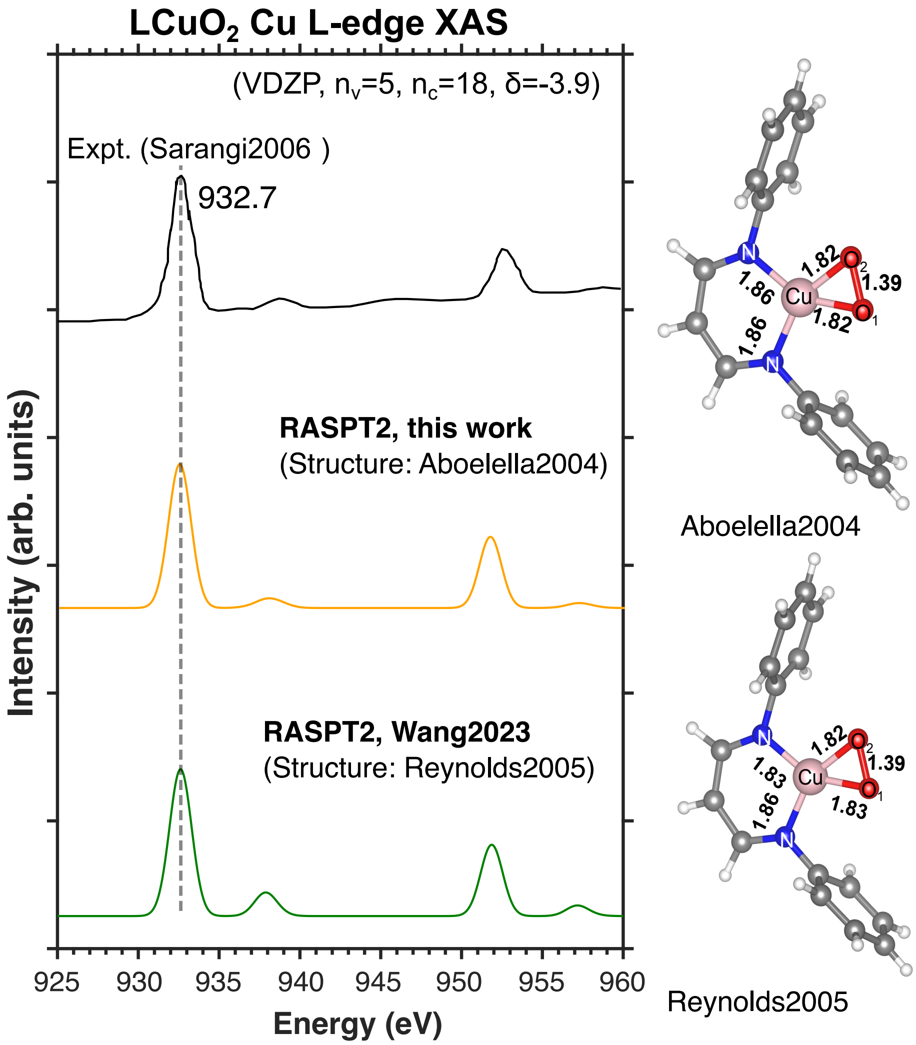

FIG. S5: **Structural dependence of Cu L-edge spectra.** Cu $L_{2,3}$-edge XAS spectra of $LCuO_2$ simulated for geometries from Reynolds et al.[6] and Aboelella et al.[7] crystal structures. RASPT2 calculations used consistent models and are compared with experimental data.[8] The spectrum for the Reynolds structure (green) is adapted from our previous work[9], while the Aboelella structure spectrum (orange) was computed in this work. Both structures yield similar spectra, validating the use of Aboelella's symmetric structure in the current study.

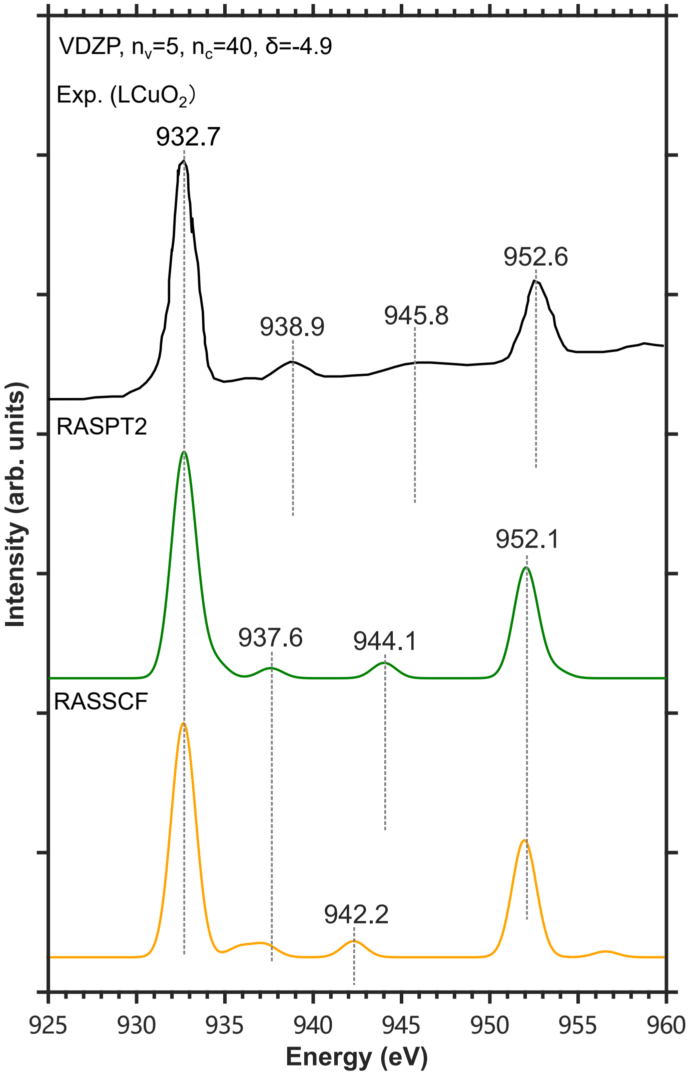

FIG. S6: **Dynamic correlation effects on Cu L-edge XAS.** Simulated Cu $L_{2,3}$-edge XAS spectra of CuO_2^+ structure **2a** computed using RASSCF and RASPT2 methods. Theoretical spectra are shifted by $\delta = -4.9$ eV to align with experimental data. Both methods yield nearly identical spectra, indicating minimal sensitivity to dynamic correlation.

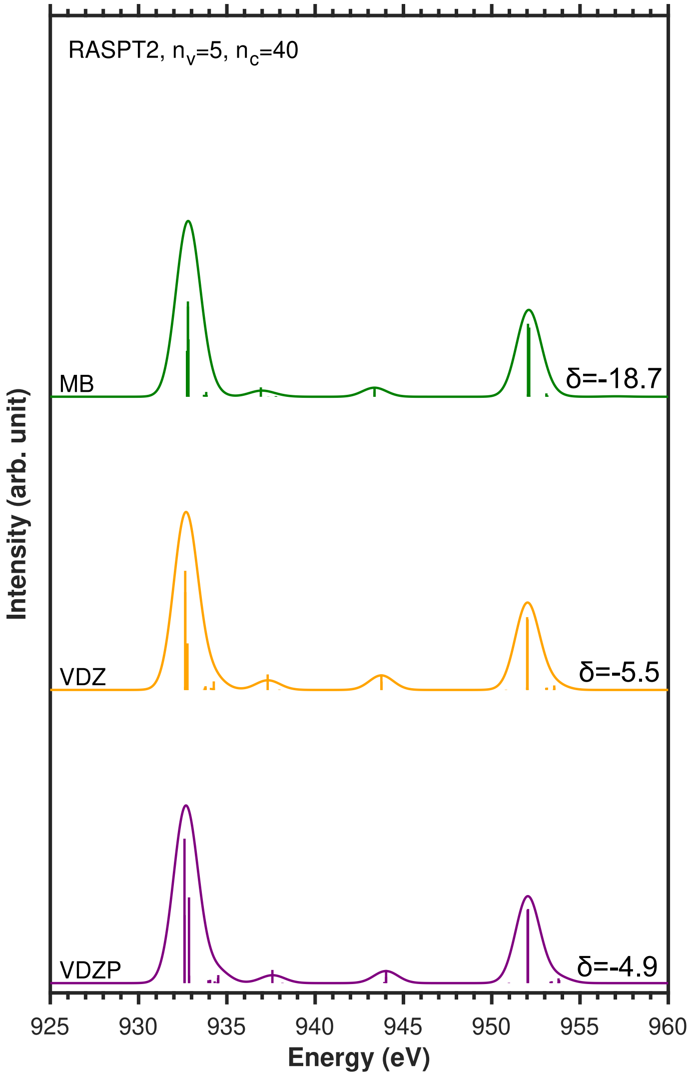

FIG. S7: **Basis set effects on Cu L-edge XAS.** Cu $L_{2,3}$-edge XAS spectra of CuO_2^+ structure **2a** computed with different ANO-RCC basis sets. Spectra show consistent shapes across basis sets, with VDZP selected for optimal balance of accuracy and computational cost.

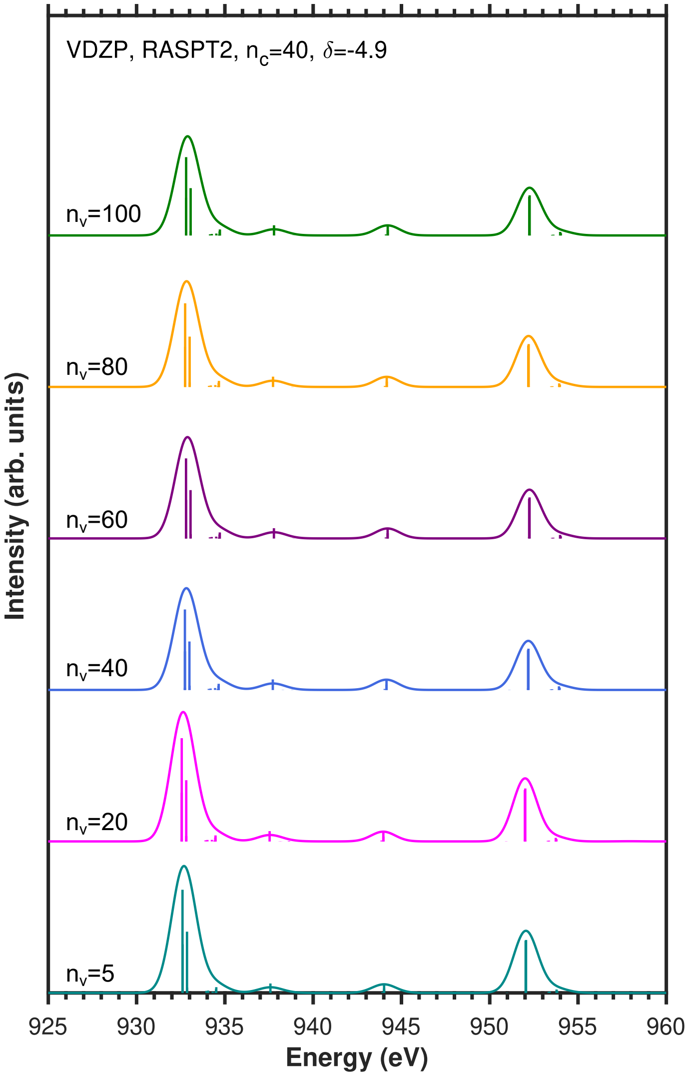

FIG. S8: **Valence state averaging effects on Cu L-edge XAS.** Cu $L_{2,3}$-edge XAS spectra of CuO_2^+ structure **2a** computed with different numbers of valence states (n_v). Spectra show negligible variation, confirming convergence with $n_v = 5$.

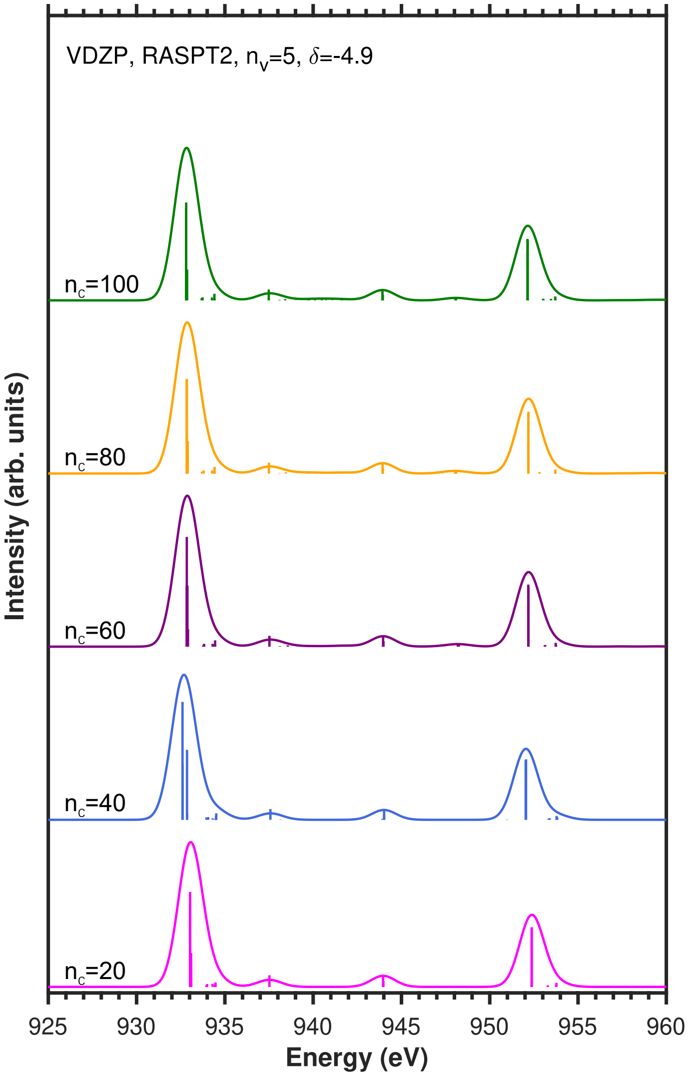

FIG. S9: **Core-excited state averaging effects on Cu L-edge XAS.** Cu $L_{2,3}$-edge XAS spectra of CuO_2^+ structure **2a** computed with different numbers of core-excited states (n_c). Spectral convergence is achieved with $n_c = 40$.

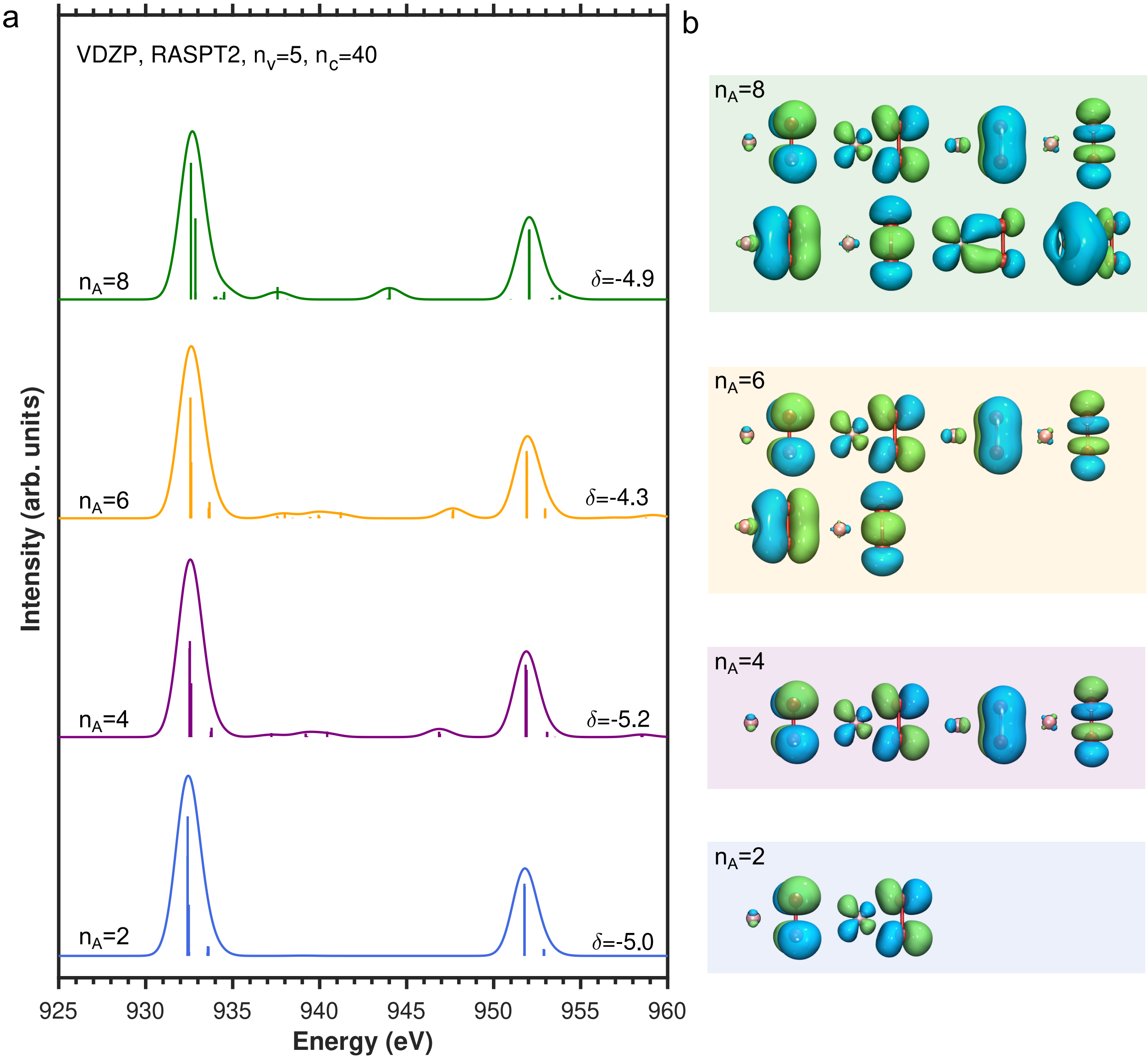

FIG. S10: **Active space size effects on Cu L-edge XAS.** (a) Cu $L_{2,3}$-edge XAS spectra of $CuO_2{}^+$ structure **2a** computed with different numbers of active orbitals (n_A). (b) Corresponding RAS2 active orbitals. Larger active spaces better resolve minor spectral features while maintaining qualitative agreement.

---

[1] Epifanovsky, E. *et al.* Software for the Frontiers of Quantum Chemistry: An Overview of Developments in the Q-chem 5 Package. *J. Chem. Phys.* **155**, 84801 (2021).

[2] Mardirossian, N. & Head-Gordon, M. ωB97M-V: A Combinatorially Optimized, Range-Separated Hybrid, Meta-GGA Density Functional with VV10 Nonlocal Correlation. *J. Chem. Phys.* **144**, 214110 (2016).

[3] Weigend, F., Furche, F. & Ahlrichs, R. Gaussian Basis Sets of Quadruple Zeta Valence Quality for Atoms H–Kr. *J. Chem. Phys.* **119**, 12753–12762 (2003).

[4] Weigend, F. & Ahlrichs, R. Balanced Basis Sets of Split Valence, Triple Zeta Valence and Quadruple Zeta Valence Quality for H to Rn: Design and Assessment of Accuracy. *Phys. Chem. Chem. Phys.* **7**, 3297 (2005).

[5] Ros, P. & Schuit, G. C. A. Molecular Orbital Calculations on Copper Chloride Complexes. *Theor. Chim. Acta* **4**, 1–12 (1966).

[6] Reynolds, A. M., Gherman, B. F., Cramer, C. J. & Tolman, W. B. Characterization of a 1:1 Cu-O_2 Adduct Supported by an Anilido Imine Ligand. *Inorg. Chem.* **44**, 6989–6997 (2005).

[7] Aboelella, N. W. *et al.* Dioxygen Activation at a Single Copper Site: Structure, Bonding, and Mechanism of Formation of 1:1 Cu-O_2 Adducts. *J. Am. Chem. Soc.* **126**, 16896–16911 (2004).

[8] Sarangi, R. *et al.* X-Ray Absorption Edge Spectroscopy and Computational Studies on $LCuO_2$ Species: superoxide-Cu^{II} versus peroxide-Cu^{III} Bonding. *J. Am. Chem. Soc.* **128**, 8286–8296 (2006).

[9] Wang, S.-Y., Zhang, J.-R., Guo, M. & Hua, W. Interpreting the Cu–O_2 Antibonding Nature in Two Cu–O_2 Complexes from Cu L-edge X-Ray Absorption Spectra. *Inorg. Chem.* **62**, 17115–17125 (2023).